Monthly Notices
of the
ROYAL ASTRONOMICAL SOCIETY

MNRAS **469,** 4283–4291 (2017)
Advance Access publication 2017 May 15

doi:10.1093/mnras/stx1167

Large 21-cm signals from AGN-dominated reionization

Girish Kulkarni,[1]★ Tirthankar Roy Choudhury,[2] Ewald Puchwein[1] and Martin G. Haehnelt[1]

[1]*Institute of Astronomy and Kavli Institute of Cosmology, University of Cambridge, Madingley Road, Cambridge CB3 0HA, UK*
[2]*National Centre for Radio Astrophysics, Tata Institute of Fundamental Research, Post Bag 3, Ganeshkhind, Pune 411007, India*

Accepted 2017 May 10. Received 2017 May 9; in original form 2017 January 16

ABSTRACT

We present predictions for the spatial distribution of 21-cm brightness temperature fluctuations from high-dynamic-range simulations for active galactic nucleus (AGN)-dominated reionization histories that have been tested against available Lyα and cosmic microwave background (CMB) data. We model AGNs by extrapolating the observed $M_{\rm bh} - \sigma$ relation to high redshifts and assign them ionizing emissivities consistent with recent UV luminosity function measurements. We assess the observability of the predicted spatial 21-cm fluctuations in the late stages of reionization in the limit in which the hydrogen 21-cm spin temperature is significantly larger than the CMB temperature. Our AGN-dominated reionization histories increase the variance of the 21-cm emission by a factor of up to 10 compared to similar reionization histories dominated by faint galaxies, to values close to 100 mK^2 at scales accessible to experiments ($k \lesssim 1$ cMpc$^{-1}\,h$). This is lower than the sensitivity reached by ongoing experiments only by a factor of about 2 or less. When reionization is dominated by AGNs, the 21-cm power spectrum is enhanced on all scales due to the enhanced bias of the clustering of the more massive haloes and the peak in the large scale 21-cm power is strongly enhanced and moved to larger scales due to bigger characteristic bubble sizes. AGN-dominated reionization should be easily detectable by Low Frequency Array (and later Hydrogen Epoch of Reionization Array and Phase 1 of the Square Kilometre Array) at their design sensitivity, assuming successful foreground subtraction and instrument calibration. Conversely, these could become the first non-trivial reionization scenarios to be ruled out by 21-cm experiments, thereby constraining the contribution of AGNs to reionization.

Key words: galaxies: active – galaxies: high-redshift – intergalactic medium – quasars: general – dark ages, reionization, first stars.

1 INTRODUCTION

Hydrogen reionization is generally thought to occur at redshifts $z \sim 6$–15 by Lyman continuum photons that are widely believed to be produced by young stars in low-mass galaxies (Mitra, Choudhury & Ferrara 2015). However, the idea that active galactic nuclei (AGNs) could have been the dominant source of ionizing radiation during the epoch of reionization has recently gained traction again (Chardin et al. 2015; Giallongo et al. 2015; Madau & Haardt 2015; D'Aloisio et al. 2016; Khaire et al. 2016; Mitra, Choudhury & Ferrara 2016; Chardin, Puchwein & Haehnelt 2017).

The resurgence of AGNs as a credible source of ionizing photons at high redshift is due to a number of recent developments. First, the claimed discovery of 19 low-luminosity ($M_{1450} > -22.6$) AGNs between redshifts $z = 4.1$ and 6.3 by Giallongo et al. (2015) using a novel X-ray/NIR selection criterion may suggest that the faint end of the quasar UV luminosity function is steeper at these redshifts than previously thought (Hopkins, Richards & Hernquist 2007; Haardt & Madau 2012). Using far-UV spectral slopes from composite spectra of low-redshift quasars and assuming a Lyman continuum escape fraction of 100 per cent, Giallongo et al. (2015) argued that AGNs brighter than $M_{1450} = -18$ can potentially produce all of the metagalactic hydrogen photoionization rate inferred from the Lyα forest at $4 < z < 6$. Secondly, Becker et al. (2015) reported a large scatter in the Lyα opacity between different sightlines close to redshift $z = 6$. Chardin et al. (2015) showed that these opacity fluctuations extend to substantially larger scales ($\gtrsim 50\,h^{-1}$cMpc) than expected in reionization histories dominated by low-luminosity galaxies (see also Davies & Furlanetto 2016). Chardin et al. (2017) further demonstrated that opacity fluctuations on such large scales arise naturally if there is a significant

★ E-mail: kulkarni@ast.cam.ac.uk

contribution ($\gtrsim$50 per cent) of AGNs to the ionizing emissivity at the redshift of the observed opacity fluctuations ($z \sim 5.5$–6) as would be expected for an AGN luminosity that is consistent with the measurements of Giallongo et al. (2015). Thirdly, measurements of the Lyman continuum escape fraction from high-redshift galaxies are still elusive. Although high-redshift galaxies as faint as rest-frame UV magnitude $M_{\rm UV} = -12.5$ ($L \sim 10^{-3}L^*$) at $z = 6$ (Livermore, Finkelstein & Lotz 2017) and redshifts as high as $z = 11.1$ (Oesch et al. 2016) have now been reported, the escape of Lyman continuum photons has been detected in only a small number of comparatively bright ($L > 0.5L^*$) low-redshift ($z < 4$) galaxies. In these galaxies, the escape fraction is typically found to be 2–20 per cent (Vanzella et al. 2010; Boutsia et al. 2011; Siana et al. 2015; Mostardi et al. 2015; Grazian et al. 2016; Japelj et al. 2017; Micheva et al. 2017b) but reionization would require escape fraction of about 20 per cent in galaxies down to $M_{\rm UV} = -13$ (Robertson et al. 2015; Finkelstein 2016; Khaire et al. 2016). Finally, incidence of high-redshift AGNs is also consistent with the shallow bright-end slopes of the high-redshift ($z \sim 7$) UV luminosity function of galaxies relative to a Schechter-function representation (Bowler et al. 2012, 2014, 2015; Bradley et al. 2014) and the hard spectra of these bright galaxies (Stark et al. 2015a,b, 2017).

It is thus pertinent to ask what a significant contribution of AGNs to the ionizing emissivity during reionization implies for the search for the 21-cm signal from the epoch of reionization. In this paper, we therefore present predictions for the 21-cm power spectrum from redshifts $z = 7$–10 in models of reionization in which the hydrogen-ionizing emissivity is dominated by AGNs and compare them to galaxy-dominated models. We use the excursion set method to derive the large-scale ionization field in high-dynamic-range cosmological simulations, using the calibration scheme developed by Choudhury et al. (2015) to incorporate 21-cm signal from self-shielded high-density regions (Kulkarni et al. 2016). AGNs are modelled by placing black holes in haloes by assuming the $z = 0$ $M_{\rm bh}$–σ relation between the black hole mass and the bulge stellar velocity dispersion (Kulkarni & Loeb 2012; Ferrarese 2002). We describe our simulations and the AGN model in Section 2. Section 3 presents our predictions for the 21-cm signal and its observability in ongoing and future experiments. We discuss the case for and against reionization by AGNs in Section 4 and end by summarizing our results in Section 5. Our ΛCDM cosmological model has $\Omega_{\rm b} = 0.0482$, $\Omega_{\rm m} = 0.308$, $\Omega_\Lambda = 0.692$, $h = 0.678$, $n = 0.961$, $\sigma_8 = 0.829$ and $Y_{\rm He} = 0.24$ (Planck Collaboration 2014).

2 MODELS OF AGN-DOMINATED REIONIZATION

Our 21-cm predictions are based on cosmological hydrodynamical simulations that are part of the Sherwood simulation suite (nottingham.ac.uk/astronomy/sherwood; Bolton et al. 2017). Sources of ionizing radiation are placed in haloes identified in the simulation and an ionization field is obtained using the well-known excursion set approach. This ionization field is then calibrated to a given reionization history, while accounting for residual neutral gas in high-density areas within ionized regions. The reionization histories used for calibration are chosen carefully such that they are consistent with Lyα and cosmic microwave background (CMB) data as described in Choudhury et al. (2015). In this manner, our models self-consistently predict, at high resolution, the large-scale distribution of neutral hydrogen for reionization histories consistent with constraints during the late stages of reionization.

Kulkarni et al. (2016) provide more details of our implementation of the excursion set method of deriving the large-scale ionization field and its subsequent calibration to Lyα and CMB data. We recapitulate an outline of the method here to mention important parameter values and set up notation. We obtain the gas density field from the underlying cosmological simulation by projecting the relevant particles on to a grid using the cloud-in-cell scheme. From the gas density field, we derive the ionization field corresponding to a distribution of sources with specific ionizing emissivities. Denoting the total number of ionizing photons produced by a halo of mass M as $N_\gamma(M)$, a grid cell at position $\mathbf{x}$ is ionized if the condition

$$\zeta_{\rm eff}\, f(\mathbf{x}, R) \geq 1 \tag{1}$$

is satisfied in a spherical region centred on the cell for some radius R (Furlanetto, Zaldarriaga & Hernquist 2004; Choudhury, Haehnelt & Regan 2009; Mesinger, Furlanetto & Cen 2011). Here,

$$f \propto \rho_{\rm m}(R)^{-1} \int_{M_{\rm min}}^{\infty} {\rm d}M \left.\frac{{\rm d}N}{{\rm d}M}\right|_R N_\gamma(M), \tag{2}$$

where $\rho_{\rm m}(R)$ is the average matter density and ${\rm d}N/{\rm d}M|_R$ is the halo mass function in the sphere of radius R and $M_{\rm min}$ is the minimum mass of haloes that emit Lyman continuum photons. The quantity f is proportional to the collapsed fraction $f_{\rm coll}$ into haloes of mass $M > M_{\rm min}$ if $N_\gamma(M) \propto M$. The parameter $\zeta_{\rm eff}$ here is the effective ionizing efficiency, which corresponds to the number of photons in the intergalactic medium (IGM) per hydrogen atom in stars, compensated for the number of hydrogen recombinations in the IGM. It is the only parameter that determines the large scale ionization field in this approach. Cells that do not satisfy the criterion in equation (1) are neutral. We denote the ionized volume fraction in a cell i as Q_i. The total volume-weighted ionized fraction is then $Q_{\rm V} \equiv \sum_i Q_i/n_{\rm cell}$, where $n_{\rm cell}$ is the total number of grid cells.

We calibrate the large-scale ionization field obtained by the above procedure to a chosen reionization history, incorporating inhomogeneities within ionized regions, using the method developed by Choudhury et al. (2015). We begin by fixing a reionization model, which is specified by the redshift evolution of the volume-weighted ionization fraction $Q_{\rm V}$. Our simulated ionization field is calibrated to the given reionization model in two steps. In the first step, the effective ionization parameter $\zeta_{\rm eff}$ is tuned to get the volume-weighted ionization fraction predicted by the reionization history at the corresponding redshift. In the second step, we obtain the photoionization rate distribution within the ionized regions by solving the globally averaged radiative transfer equation

$$\frac{{\rm d}Q_{\rm V}}{{\rm d}t} = \frac{\dot{n}_{\rm ion}}{n_{\rm H}} - \frac{Q_{\rm V}}{t_{\rm rec}} \tag{3}$$

for the photoionization rate $\Gamma_{\rm HI}$. Here, $\dot{n}_{\rm ion}$ is the average comoving photon emissivity, $n_{\rm H}$ is the average hydrogen density and $t_{\rm rec}$ is the recombination time-scale. We implement self-shielding in ionized regions using the fitting function obtained by Rahmati et al. (2013) from radiative transfer simulations.[1] This creates cells with excess neutral hydrogen fraction, thereby reducing the mean free path of Lyman continuum photons. The mean free path $\lambda_{\rm mfp}$ enters

[1] This self-shielding is insensitive to the presence of hard ionizing photons, such as those from AGNs, due to diminished ionization cross-section (Rahmati et al. 2013).

equation (3) via $\dot{n}_{\rm ion}$, which is related to the photoionization rate by (Kuhlen & Faucher-Giguère 2012; Becker & Bolton 2013)

$$\dot{n}_{\rm ion} = \frac{\Gamma_{\rm HI} Q_{\rm V}}{(1+z)^2 \sigma_{\rm H} \lambda_{\rm mfp}} \left(\frac{\alpha_{\rm b} + 3}{\alpha_{\rm s}} \right), \tag{4}$$

where $\sigma_{\rm H}$ is the hydrogen photoionization cross-section, $\alpha_{\rm s}$ is the spectral index of the ionizing sources at $\lambda < 912$ Å and $\alpha_{\rm b}$ is the spectral index of the ionizing 'background' within ionized regions.

The Sherwood simulation suite has been run using the energy- and entropy-conserving TreePM smoothed particle hydrodynamical code P-GADGET-3, which is an updated version of the GADGET-2 code (Springel, Yoshida & White 2001; Springel 2005). Our base simulation was performed in a periodic cube of length 160 h^{-1}cMpc on a side. The number of gas and dark matter particles were both initially 2048^3. This corresponds to a dark matter particle mass of $M_{\rm dm} = 3.44 \times 10^7\ h^{-1}\ {\rm M}_\odot$ and gas particle mass of $M_{\rm gas} = 6.38 \times 10^6\ h^{-1}\ {\rm M}_\odot$. In the redshift range relevant to this paper, we use snapshots of the particle positions at $z = 10$, 8 and 7. Haloes are identified using the friends-of-friends algorithm. At $z = 7$, the minimum halo mass in our simulation is $2.3 \times 10^8\ h^{-1}\ {\rm M}_\odot$; the maximum halo mass is $3.1 \times 10^{12}\ h^{-1}\ {\rm M}_\odot$.

To model ionizing emission by AGNs, we assume that in high-mass haloes that host luminous AGNs, the total number of photons N_γ is proportional to the black hole mass $M_{\rm bh}$. In order to estimate the mass of black holes in these haloes, we follow the approach of Kulkarni & Loeb (2012) and employ the $M_{\rm bh}$–σ relation (cf. Mao & Kim 2016). The virial velocity (defined as the circular velocity at virial radius) for a halo of mass M at redshift z is given by

$$v_{\rm c} = 23.4\,{\rm km\,s^{-1}} \left(\frac{M}{10^8 h^{-1}{\rm M}_\odot} \right)^{1/3} \times \left[\frac{\Omega_{\rm m}}{\Omega_{\rm m}^z} \frac{\Delta_{\rm c}}{18\pi^2} \right]^{1/6} \left(\frac{1+z}{10} \right)^{1/2}, \tag{5}$$

where

$$\Omega_{\rm m}^z = \frac{\Omega_{\rm m}(1+z)^3}{\Omega_{\rm m}(1+z)^3 + \Omega_\Lambda + \Omega_{\rm k}(1+z)^2}, \tag{6}$$

and $\Delta_{\rm c}$ is the overdensity of the halo relative to the critical density, given by

$$\Delta_{\rm c} = 18\pi^2 + 82d - 39d^2, \tag{7}$$

where $d = \Omega_{\rm m}^z - 1$ (Barkana & Loeb 2001). Further, we equate the halo virial velocity with the circular velocity $v_{\rm c}$ of its constituent spheroid and obtain the velocity dispersion of the spheroid using the relation (Ferrarese 2002)

$$v_{\rm c} \approx 314 \left[\frac{\sigma}{208\,{\rm km\,s^{-1}}} \right]^{0.84} {\rm km\,s^{-1}}. \tag{8}$$

Equation (8) combined with the measured $M_{\rm bh}$–σ relation at redshift $z = 0$ (Tremaine et al. 2002)

$$\frac{\sigma}{208\,{\rm km\,s^{-1}}} \approx \left[\frac{M_{\rm bh}}{1.56 \times 10^8 {\rm M}_\odot} \right]^{1/4.02}, \tag{9}$$

gives

$$\frac{M_{\rm bh}}{10^8 {\rm M}_\odot} = 0.12 \left(\frac{M_{\rm halo}}{10^{12} {\rm M}_\odot} \right)^{1.6} \left[\frac{\Omega_{\rm m}}{\Omega_{\rm m}^z} \frac{\Delta_{\rm c}}{18\pi^2} \right]^{0.8} (1+z)^{2.4}. \tag{10}$$

We assume that haloes with mass below a threshold mass $M_{\rm q}$ have $N_\gamma(M) = N_\gamma^{\rm gal}(M) \propto M_{\rm halo}$. Ionizing photons from these low-mass haloes are sourced by star formation.[2] On the other hand, high-mass haloes with mass greater than the threshold $M_{\rm q}$ have $N_\gamma(M) = N_\gamma^{\rm agn}(M) \propto M_{\rm bh}$, where $M_{\rm bh}$ is given by equation (10). These high-mass haloes produce ionizing photons due to AGNs. The ratio

$$r \equiv \frac{\int_{M_{\rm q}}^{M_{\rm max}} {\rm d}M\, N_\gamma^{\rm agn}(M)\, {\rm d}N/{\rm d}M}{\int_{M_{\rm min}}^{M_{\rm q}} {\rm d}M\, N_\gamma^{\rm gal}(M)\, {\rm d}N/{\rm d}M}, \tag{11}$$

quantifies the relative photon contribution of AGNs and galaxies. Our AGN models are thus described by two parameters r and $M_{\rm q}$. (Appendix gives further details on our AGN-ionizing emissivity model.)

In our fiducial AGN-dominated model, we fix the value of the threshold mass $M_{\rm q}$ to that corresponding to a circular velocity of $v_{\rm c} = 175$ km s^{-1}. (We will discuss the effect on our results of changing this threshold to $v_{\rm c} = 150$ km s^{-1} and $v_{\rm c} = 200$ km s^{-1} below.) At lower circular velocities, cold gas mass available to grow supermassive black holes can decrease rapidly due to an increasing effect of supernova feedback (e.g. Kauffmann & Haehnelt 2000; Haehnelt & Kauffmann 2002; Brook et al. 2012). This is reflected in a drop in the black hole mass function for black hole masses smaller than $M_{\rm bh} \sim 10^7\,{\rm M}_\odot$, particularly for $z > 1$ (Merloni & Heinz 2008; Kelly & Merloni 2012). With $M_{\rm q}$ fixed, a desired total AGN emissivity is achieved in the model by setting the value of the parameter r. We calibrate the AGN-emissivity evolution to values close to the fit by Madau & Haardt (2015) to the integrated 1 Ry emissivity from AGNs down to UV luminosities of $0.01L_*$. This emissivity evolution is shown by the red curve in the right-hand panel of Fig. 1. In this panel, red filled circles denote ionizing emissivity from AGNs in our model; red open circles refer to the total ionizing emissivity, which also includes contribution from star-forming galaxies. The ionizing emissivity of AGNs in our model closely matches that from the model of Madau & Haardt (2015). We also have some contribution to $\dot{n}_{\rm ion}$ from star-forming galaxies in our model, particularly at $z = 10$, as seen from the red open circles in Fig. 1. For comparison, the grey points in Fig. 1 show the photon emissivity in the galaxy-dominated 'Late/Default' model of Kulkarni et al. (2016).

Having chosen a source model, we now need to choose a suitable reionization history to calibrate our simulation. As discussed above in relation to equation (3), this calibration will provide us with the photoionization rate and ionized hydrogen fraction throughout our simulation box. The AGN-dominated ionizing emissivity evolution considered by Madau & Haardt (2015) gives rise to a reionization history that is very close to the 'Very Late' reionization history as described by Kulkarni et al. (2016). For ease of comparison, we thus choose this reionization history to calibrate our simulation. The red curve in the left-hand panel of Fig. 1 shows the evolution of the volume-weighted ionized fraction $Q_{\rm V}$ in this Very Late model. For comparison, the grey curve in this panel shows the evolution of $Q_{\rm V}$ in the 'Late/Default' model of Kulkarni et al. (2016). In the Very Late model, ionized regions overlap and the Universe is completely reionized at $z = 6$, similar to the Late/Default model, but $Q_{\rm V}$ evolves more rapidly at $z > 6$ (Kulkarni et al. 2016). This model agrees reasonably well with the background photoionization rate determined from the Lyα forest at $z < 6$ (Faucher-Giguère et al.

[2] While AGNs have harder spectra than star-forming galaxies, the effect of harder photons on the structure of the hydrogen ionization fronts is small (Thomas & Zaroubi 2008; Ghara, Choudhury & Datta 2015; Kakiichi et al. 2016). The excursion set method therefore remains applicable.

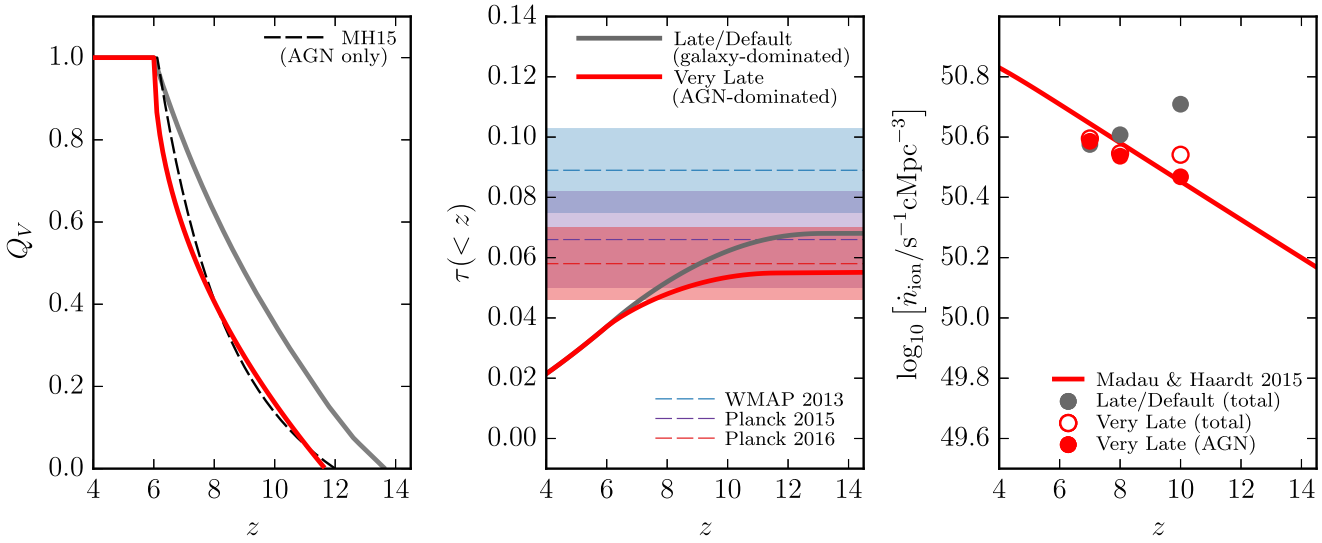

Figure 1. Evolution of the volume-weighted ionization fraction $Q_{\rm V}$ (left-hand panel), the electron scattering optical depth τ (middle panel), and the hydrogen-ionizing emissivity $\dot{n}_{\rm ion}$ (right-hand panel) in the AGN-dominated 'Very Late' reionization model considered in this paper and the galaxy-dominated 'Late/Default' model of Kulkarni et al. (2016). The AGN-dominated model is shown by red curves in left-hand and middle panels, and red points and open circles in the right-hand panel. The galaxy-dominated model is shown by the grey curves and points. The dashed black curve in the left-hand panel shows the model of Madau & Haardt (2015), which includes emission only from AGNs; the red curve in the right-hand panel shows the corresponding emissivity. In the right-hand panel, red filled circles denote ionizing emissivity from AGNs in our model; red open circles refer to the total ionizing emissivity, which also includes contribution from star-forming galaxies.

2009; Becker & Bolton 2013) and from quasar proximity zones at $z \sim 6$ (Calverley et al. 2011; Wyithe & Bolton 2011), albeit with notable differences (Chardin et al. 2015; Puchwein et al. 2015). The value of the electron scattering optical depth to the last scattering surface in this model is $\tau = 0.055$, in good agreement with the most recent Planck measurement ($\tau = 0.058 \pm 0.012$; Planck Collaboration 2016), as seen in the middle panel of Fig. 1.

3 RESULTS: 21-CM SIGNAL

The top panel of Fig. 2 shows the evolution of the 21-cm brightness temperature from redshift $z = 10$–6 in our fiducial $v_{\rm c} > 175$ km s^{-1} AGN-dominated model. The 21-cm brightness temperature is approximated as

$$T_{\rm b}(\mathbf{x}) = \overline{T}_{\rm b} x_{\rm HI}(\mathbf{x})\Delta(\mathbf{x}), \tag{12}$$

where the mean temperature $\overline{T}_{\rm b} \approx 22\,{\rm mK}[(1+z)/7]^{1/2}$ (Choudhury et al. 2009). The above relation neglects the impact of redshift space distortions due to peculiar velocities and possible fluctuations in the spin temperature, i.e. it implicitly assumes that the spin temperature is much greater than the CMB temperature and that the Lyα coupling is sufficiently complete throughout the IGM. This is a good approximation in the redshift range considered here, when the global ionized fraction is greater than a few per cent (Pritchard & Loeb 2012; Majumdar et al. 2014; Ghara et al. 2015). For comparison, the middle panel of Fig. 2 shows the evolution of the 21-cm brightness in the galaxy-dominated Very Late model considered by Kulkarni et al. (2016). The reionization history of this model is identical to that of our AGN-dominated model, so the differences in the brightness distribution between the top and middle panels of Fig. 2 arise solely due to differences in the source model. The AGN-dominated model has fewer, larger and more clustered ionized regions than the galaxy-dominated model (cf. McQuinn et al. 2007). Fig. 2 also shows the galaxy-dominated Late/Default model of Kulkarni et al. (2016) in the bottom panel. The source model as well as the reionization history is now different from our AGN-dominated model. This is reflected in a strikingly different morphology of 21-cm bright regions.

We derive the power spectrum of the 21-cm fluctuations in our model as

$$\Delta^2_{21}(k) = \frac{k^3}{2\pi^2} \cdot \frac{\langle \widetilde{T}_{\rm b}^{\,2}(k)\rangle}{V_{\rm box}}, \tag{13}$$

where $\widetilde{T}_{\rm b}(k)$ is the Fourier transform of the brightness temperature defined in equation (12), the average is over the simulation box and $V_{\rm box} = (160\,{\rm cMpc}\,h^{-1})^3$ is the comoving box volume. Fig. 3 shows our main results at redshifts $z = 7$, 8 and 10 in its left-hand, middle and right-hand panels, respectively. The red curve in all panels shows the 21-cm power spectrum in our fiducial AGN-dominated model, in which AGNs are hosted by haloes with $v_{\rm c} > 175$ km s^{-1}. The power spectrum is characterized by a bump at large scales and an increase towards the smallest scales. At redshifts $z = 7$–10 shown, the bump occurs at $k \sim 0.2$ cMpc^{-1} h and has an amplitude of approximately $\Delta^2_{21} \sim 40$–70 mK^2. This is significantly higher than in the galaxy-dominated models. (Note that $k = 0.2$ cMpc^{-1} h corresponds to a length scale of $30\,h^{-1}$ cMpc, which is well-sampled in our simulation cube, which is $160\,h^{-1}$ cMpc on each side.) We can compare the large-scale power in our AGN-dominated model with that in the galaxy-dominated Very Late model in Fig. 3, in which the galaxy-dominated model is shown by the dashed grey curves. The large-scale power in the AGN-dominated model is larger than that in the galaxy-dominated model by factor of 2 at $z = 7$ and a factor of 10 at $z = 10$. As we will see below, this enhancement is due to the enhanced size and clustering of ionized regions, which is also visually apparent in Fig. 2. The large-scale 21-cm power in our fiducial AGN-dominated model is also higher than the large-scale power in the Late/Default model of Kulkarni et al. (2016). Power spectra from the latter model are shown by the solid grey curves in Fig. 3. The enhancement factor here is about 3 at $z = 7$ and 2 at

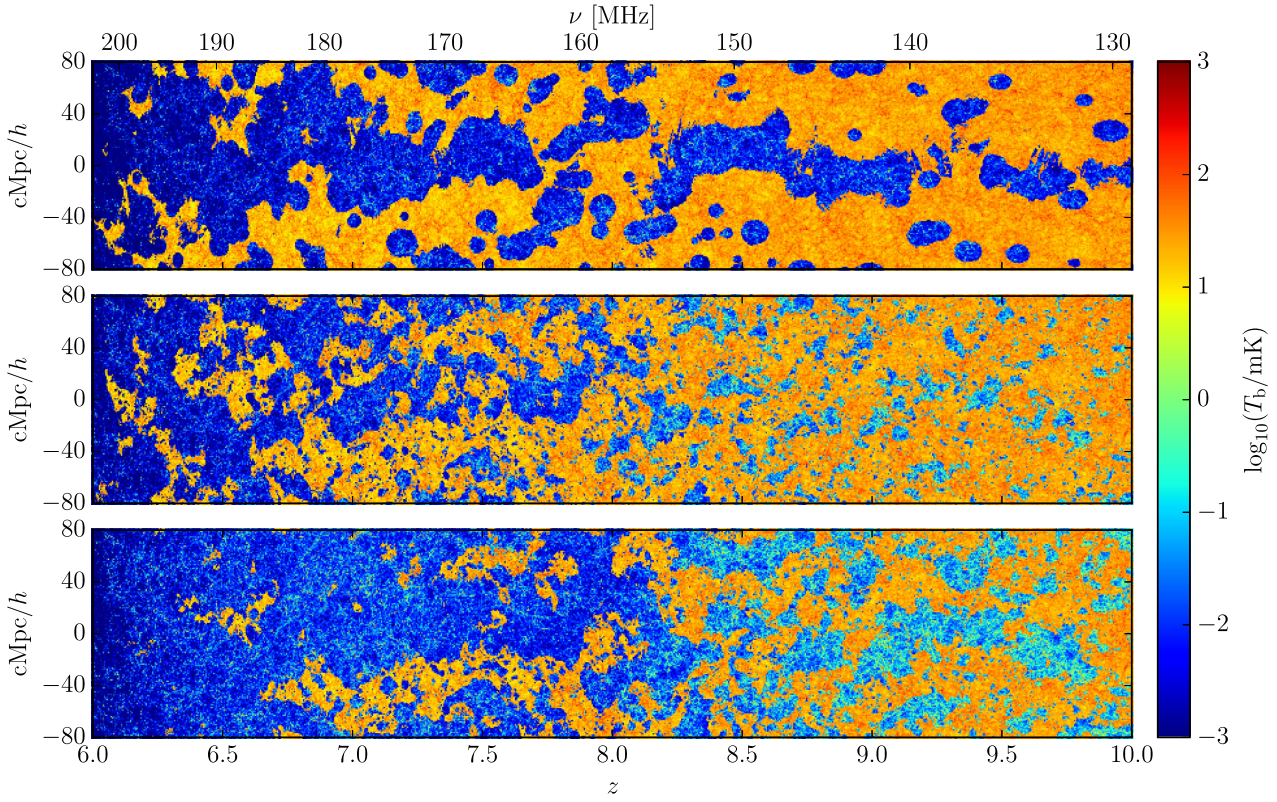

Figure 2. Evolution of the 21-cm brightness temperature distribution from redshift $z = 10$–6 in the AGN-dominated Very Late model (top panel) introduced in this paper, the galaxy-dominated Very Late model (middle panel) from Kulkarni et al. (2016), and the galaxy-dominated Late/Default model (bottom panel) also from Kulkarni et al. (2016).

$z = 10$. At redshifts $z = 8$ and 10, the Late/Default model has higher power than the galaxy-dominated Very Late model at large scales, because of the higher Q_V, which translates to larger bubble size, as is evident from Fig. 2.

In Fig. 3, we also show the effect of changing the circular velocity threshold for AGN-hosting haloes. The red curve in this figure shows the 21-cm power spectrum in our fiducial AGN-dominated model, when AGNs are hosted by haloes with $v_c > 175$ km s^{-1}. The blue and green curves show the power spectra when the circular velocity threshold is changed to 200 km s^{-1} and 150 km s^{-1}, respectively. The main effect of this change on the large-scale 21-cm power is to shift the position of the bump. As all three models are calibrated to the same Very Late reionization history, they have identical ionization fraction Q_V at each redshift. Therefore, when the circular velocity threshold is reduced, the number of AGN-hosting haloes increases and consequently, in order to hold Q_V fixed, the size of individual ionized regions decreases. This moves the bump in the 21-cm power spectrum to smaller scales (cf. Iliev et al. 2012).

The thin diagonal lines in each panel of Fig. 3 show sensitivities set by thermal noise for five ongoing and upcoming 21-cm experiments: the Precision Array for Probing the Epoch of Reionization (PAPER; Parsons et al. 2014), Murchison Widefield Array (MWA; Bowman et al. 2013; Tingay et al. 2013), Low-Frequency Array (LOFAR; van Haarlem et al. 2013; Pober et al. 2014), Hydrogen Epoch of Reionization Array (HERA; Pober et al. 2014) and the low-frequency instrument from Phase 1 of the Square Kilometre Array (SKA1-LOW). We consider 1000 h of observations and use experimental parameters identical to those considered by Kulkarni et al. (2016). Note that the sample variance from the limited number of k modes measured in the survey volume also limits the sensitivity of the experiment. The sample variance scales as $\Delta^2(k)/\sqrt{N}$ and, due to the small amplitude of the power spectrum, is smaller (<1 mK^2) than the thermal noise at all redshifts for all experiments considered here. Also note that we assume perfect foreground subtraction in this discussion. Foreground subtraction and calibration residuals will reduce the experimental sensitivity (Bernardi et al. 2009; Pober et al. 2013; Dillon et al. 2014). Due to the relatively smooth dependence of astrophysical foregrounds on frequency, this reduction in sensitivity particularly affects small k values.

Due to limited baselines, current and upcoming 21-cm experiments are only sensitive to large scales. None of the experiments are sensitive to 21-cm power at $k \gtrsim 1$ cMpc^{-1} h. SKA1-LOW and HERA have the highest sensitivities primarily due to a large number of antenna elements. In the galaxy-dominated Late/Default model, at $z = 10$ (129 MHz), the signal-to-noise ratio (SNR) is ∼100 for these two experiments at $k \sim 0.1$ cMpc^{-1} h. This is enhanced by a further factor of ∼2 in the AGN-dominated model. At $z = 7$ (178 MHz), the enhancement is by a factor of ∼3. LOFAR is sensitive at scales corresponding to $k \lesssim 0.2$ cMpc^{-1} h at $z = 10$ (129 MHz) and $k \lesssim 0.5$ cMpc^{-1} h at $z = 7$ (178 MHz). At $k \sim 0.1$ cMpc^{-1} h, the expected SNR for LOFAR is ∼10 at $z = 10$ and ∼50 at $z = 7$, for the galaxy-dominated Late/Default model. These SNRs are also enhanced by similar factors as for SKA1-LOW and HERA in AGN-dominated models. PAPER and MWA are the least sensitive of the five experiments due to their relatively small number of antenna elements. Fig. 3 shows that while galaxy-dominated models predict small SNRs for PAPER and MWA, the AGN-dominated models do predict SNRs of ∼2 at $k \sim 0.1$ cMpc^{-1} h at redshifts $z = 7$ (178 MHz) and $z = 8$ (158 MHz). Also shown in Fig. 3

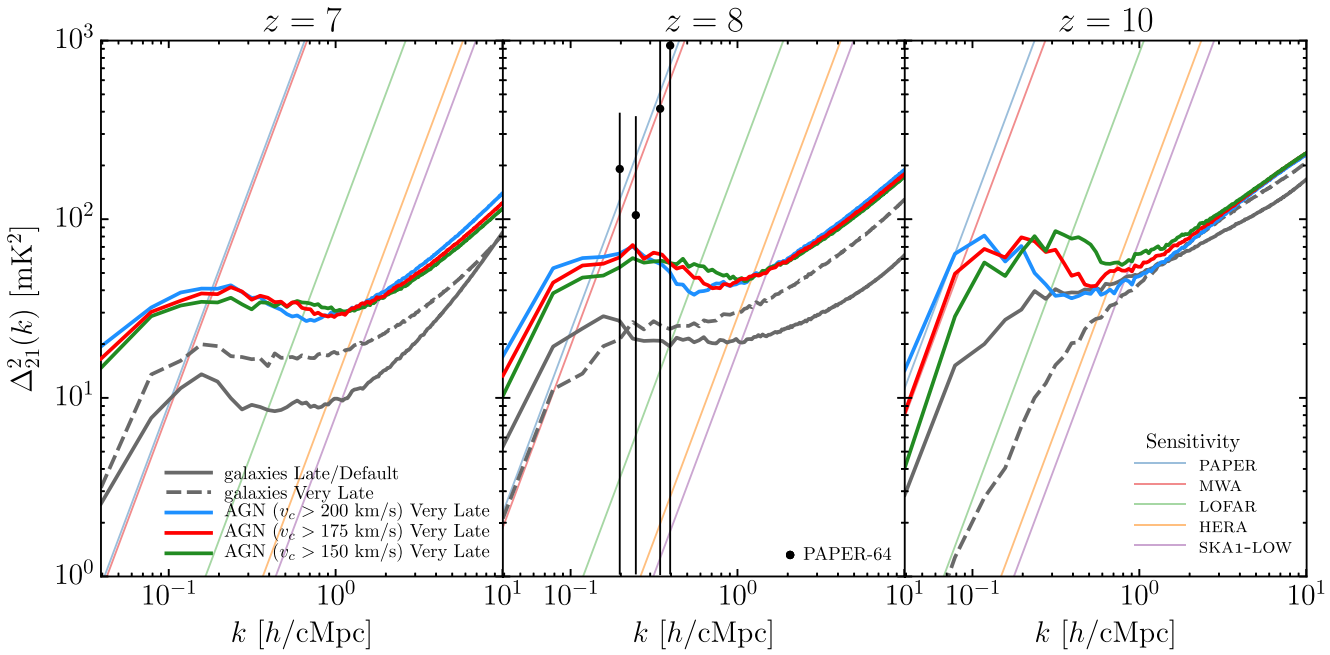

Figure 3. Red curves show the 21-cm power spectra from our fiducial AGN-dominated model, which assumes that AGNs are hosted by haloes with circular velocities greater than $v_c = 175$ km s^{-1}. Green and blue curves show the power spectra in models where this threshold is changed to 150 and 200 km s^{-1}, respectively. All three of these models are calibrated to the Very Late reionization history. Power spectra from the galaxy-dominated Late/Default model of Kulkarni et al. (2016) are shown by the solid grey curves. Dashed grey curves show power spectra from a galaxy-dominated Very Late model, also from Kulkarni et al. (2016). Thin coloured diagonal lines indicate experimental sensitivites. Data points are the measurements from the 64-element deployment of PAPER at $z = 8.4$ (Ali et al. 2015). The average ionization fraction in the Very Late model is $Q_V = 0.16$ at $z = 10$, 0.41 at $z = 8$ and 0.58 at $z = 7$. At these redshifts, the average ionization fraction in the Late/Default model is, respectively, $Q_V = 0.37$, 0.65 and 0.82.

are published measurements from the 64-element deployment of PAPER at $z = 8.4$ (Ali et al. 2015). These are within a factor of <2 of the predicted power in our AGN-dominated model. Very clearly, the 21-cm signal will be significantly easier to detect if reionization is AGN dominated. Conversely, these could become the first non-trivial models of reionization to be ruled out by 21-cm experiments, thereby constraining the contribution of AGNs to reionization and thus complementing infrared surveys.

The enhancement in the large-scale 21-cm power in AGN-dominated reionization models can be better understood by decomposing the 21-cm power spectrum into contributions from the ionization field and the underlying matter density using equation (12). This yields (Furlanetto, Zaldarriaga & Hernquist 2004; McQuinn et al. 2005; Furlanetto, Oh & Briggs 2006)

$$\Delta^2_{21}(k) = b_\delta \Delta^2_\delta(k) + b_x \Delta^2_{x_{\rm HI}}(k) + \text{cross-correlations}, \quad (14)$$

where the first and second terms on the right-hand side are the power spectra of the matter density and the ionization field, respectively, and the last term denotes the cross-power spectrum between the ionization and matter density fields. The proportionality factors b_δ and b_x are independent of k. This decomposition is shown in Fig. 4 for our fiducial AGN-dominated model and the galaxy-dominated Very Late model at $z = 8$. At small scales, the 21-cm power spectrum is proportional to the matter power spectrum. At large scales, the cross-terms in equation (14) are negative, with a magnitude of about 10 per cent of the total power. The ionization field starts contributing power at large scales, creating a bump (Furlanetto et al. 2006). This can be understood by writing the power spectrum of the ionization field in terms of the size distribution of ionized regions in a halo model approach (Furlanetto et al. 2004; McQuinn et al. 2005). The

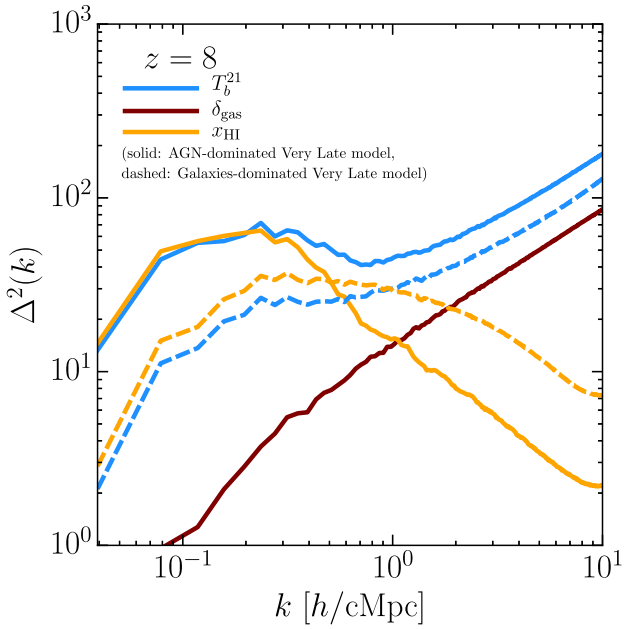

Figure 4. A decomposition of the 21-cm power spectrum (blue curve), predicted in our model, into contributions from the gas density (brown curve) and the ionization field (orange curve) at $z = 8$. Solid curves show the AGN-dominated model; dashed curves show the galaxy-dominated model. The gas density power spectrum is identical in the two models. In AGN-dominated models, the ionization field is highly clustered. This explains the enhancement in 21-cm power at large scales.

scale at which the bump appears depends on the characteristic size of ionized regions and grows with decreasing redshift. When the ionization fraction is small even the large-scale power is determined by the matter power spectrum. This is the case, for instance, in the galaxy-dominated Late/Default model at $z = 10$ in Fig. 3. However, as ionized regions grow, the bump moves to successively smaller k values. This happens with decreasing redshifts, but in our case it also happens when we put AGNs in successively higher mass haloes, that is, when we increase the threshold circular velocity of AGN-hosting haloes, because all of our AGN-dominated models are calibrated to the same Very Late reionization history. When we increase the circular velocity cut-off, the number of AGN-hosting haloes is reduced and the size of ionized regions around each AGN-hosting halo increases in order to keep $Q_{\rm V}$ fixed. This increases the spatial scale at which the power enhancement occurs. The amplitude of the peak in the power spectrum at large scales, however, does not increase arbitrarily with the circular velocity threshold. At some point, Poisson fluctuations dominate and the power approaches that corresponding to white noise. This is clearly seen in Fig. 3 in all models: the peak in large-scale power is enhanced in the AGN-dominated models relative to the galaxy-dominated models with the same (Very Late) reionization history, but when $v_{\rm c}$ is increased beyond 150 km s^{-1}, the peak simply moves to larger scales without increasing in amplitude. Thus, enhanced contribution from high-mass haloes with constant total ionization fraction increases the large scale 21-cm power up to a limit and then moves the location of the peak to larger and larger scales. This large-scale peak in the 21-cm power is perhaps the most important reionization signature for 21-cm experiments (Furlanetto et al. 2006).

4 THE CASE FOR AND AGAINST REIONIZATION BY AGNs

While interest in early reionization by X-rays from faint AGN (Meiksin & White 2004; Meiksin 2005; Srbinovsky & Wyithe 2007) was motivated by the large value of Thomson scattering optical depth measured from the first-year *WMAP* data ($\tau = 0.166^{+0.076}_{-0.071}$; Spergel et al. 2003), there are now a number of arguments favouring a significant role of normal QSOs in reionization, as discussed in Section 1: the suggestion of a rather steep faint end of the QSO luminosity function at high redshift by Giallongo et al. (2015), large Lyα opacity fluctuations at very large scales in QSO absorption spectra (Becker et al. 2015; Chardin et al. 2015; Davies & Furlanetto 2016), a lack of convincing detections of the escape of Lyman continuum photons from faint high-redshift galaxies (Vanzella et al. 2010; Boutsia et al. 2011; Mostardi et al. 2015; Robertson et al. 2015; Siana et al. 2015; Finkelstein 2016; Grazian et al. 2016; Khaire et al. 2016), and finally, the emergence of a shallow bright end of the high-redshift ($z \gtrsim 7$) galaxy luminosity function (Bowler et al. 2012, 2014, 2015; Bradley et al. 2014) with many bright galaxies showing possible AGN-like spectral signatures (Stark et al. 2015a,b, 2017). These observations all point towards a significant presence of luminous AGNs at $z > 6$, suggesting that AGNs play a major role in reionization (Chardin et al. 2015; Giallongo et al. 2015; Madau & Haardt 2015; D'Aloisio et al. 2016; Khaire et al. 2016; Mitra et al. 2016; Chardin et al. 2017).

On the other hand, however, it has also been argued that AGN-dominated reionization is in tension with several observations. D'Aloisio et al. (2016) considered the effect of AGN-dominated reionization on the Lyα opacity at $z > 5$, He II Lyα opacity at $z \sim 3.1$–3.3, and the thermal history of the IGM. In agreement with Chardin et al. (2015), these authors found that AGNs did provide a plausible explanation for the large fluctuations in the Lyα opacity at $z > 5$. However, they found that reionization of He II occurs much earlier in these AGN-dominated models (see also Mitra et al. 2016). For instance, in the model of Madau & Haardt (2015), He II reionization is complete at $z = 4.5$, compared to $z = 3$ in the standard scenario (Haardt & Madau 2012). This early Helium reionization could result in higher IGM temperatures due to the associated photoheating. The temperature of the IGM at mean density is enhanced in AGN-dominated models by factors of $\sim$2 relative to the standard models for $z = 3.5$–5, in conflict with measurements. This inconsistency could be avoided by reducing the escape fraction of 4 Ry photons in AGNs, but it is not clear if this can be achieved while requiring a 100 per cent escape fraction of 1 Ry photons in order to explain the Lyα opacity fluctuations. Further evidence against AGN-dominated reionization models has emerged from metal-line absorbers at $z \sim 6$. In their cosmological radiation hydrodynamical simulations, Finlator et al. (2016) find that the hard spectral slopes of UV backgrounds in AGN-only reionization models produce too many C IV absorption systems relative to Si IV and C II at $z \sim 6$. However, these simulations assume an $L_\nu \propto \nu^{-1.57}$ AGN spectral energy distribution (SED) at extreme UV (Vanden Berk et al. 2001; Telfer et al. 2002; Haardt & Madau 2012). This slope is marginally harder than recent measurements ($L_\nu \propto \nu^{-1.7}$) from a stack of $z \sim 2.4$ quasars (Lusso et al. 2015). Finlator et al. (2016) also find that the N(Si IV)/N(C IV) column density ratio measurements prefer a somewhat harder and more intense >4 Ry background than the standard model of Haardt & Madau (2012). Using a large sample of X-ray-selected quasars in the redshift range $z = 0$–6, Ricci et al. (2017) find that the faint end of the AGN UV luminosity function at $z \sim 6$ is likely to be much shallower than that reported by Giallongo et al. (2015). In their analysis, Ricci et al. (2017) use an AGN obscuration optical depth ($\log N_{\rm H}$) cut-off that reproduces low-redshift AGN UV luminosity functions and an X-ray-to-optical/UV luminosity ratio calibrated at redshifts $z = 0.05$–4 (Lusso et al. 2010). These authors argue that the apparent contradiction with the results of Giallongo et al. (2015) could be explained by contamination from the AGN host galaxies. It has also been recently argued that the Lyman continuum escape fraction of AGNs might not be 100 per cent as is usually assumed (Micheva, Iwata & Inoue 2017a). This may further reduce the contribution of AGNs to reionization.

A definitive understanding of the AGN contribution to reionization will perhaps only emerge with deep large-area surveys to detect faint and intermediate brightness quasars at high redshifts, such as the Subaru High-z Exploration of Low-Luminosity Quasars (SHELLQs) project (Matsuoka et al. 2016) and the VISTA Extragalactic Infrared Legacy Survey (VEILS; Hönig et al. 2017), and later with the *Wide Field Infrared Survey Telescope* (*WFIRST*; Spergel et al. 2013) and *Euclid* (Laureijs et al. 2011).

5 CONCLUSIONS

We have presented predictions of the spatial distribution of the 21-cm brightness temperature fluctuations from AGN-dominated models of reionization using high-dynamic-range cosmological hydrodynamical simulations from the Sherwood simulation suite (Bolton et al. 2017) for reionization histories motivated by constraints from Lyα absorption and emission data as well as CMB data and based on a physically motivated AGN model.

Our main conclusion is that AGN-dominated reionization histories increase the large-scale 21-cm power by factors of up to 10. Conventional models typically predict values of 10–20 mK^2 for the variance of the 21-cm brightness temperature at redshifts $z = 7$–10

at scales accessible to ongoing and upcoming experiments ($k \lesssim 1$ cMpc^{-1} h), but AGN-dominated models can increase this variance to values close to 100 mK^2. This is because AGNs reside in few highly clustered haloes, which increases the peak of the 21-cm power spectrum and moves the peak to larger scales. This bodes well for experiments that seek to detect this feature, and the predicted signal is lower than the sensitivity claimed to have been already reached by ongoing experiments by only a factor of about 2 or less.

Our models for the reionization history and Lyman continuum emissivity of AGNs suggest that detection by LOFAR (and later HERA and SKA1) should be in easy reach of their design sensitivity, albeit assuming optimistic foreground subtraction and calibration residuals. Conversely, these models could become the first non-trivial hydrogen reionization scenarios to be ruled out by experiments, thereby complementing infrared searches for high-z AGNs, and constraining the contribution of AGNs to reionization.

ACKNOWLEDGEMENTS

We thank the anonymous referee for a thoughtful referee report and acknowledge helpful discussions with Jonathan Chardin, Colin DeGraf, Kristian Finlator, Laura Keating and Dylan Nelson. Support by ERC Advanced grant 320596 'The Emergence of Structure During the Epoch of Reionization' is gratefully acknowledged. EP gratefully acknowledges support by the Kavli Foundation. We acknowledge PRACE for awarding us access to the Curie supercomputer, based in France at the Trés Grand Centre de Calcul (TGCC). This work used the DiRAC Data Centric system at Durham University, operated by the Institute for Computational Cosmology on behalf of the STFC DiRAC HPC Facility (www.dirac.ac.uk). This equipment was funded by BIS National E-infrastructure capital grant ST/K00042X/1, STFC capital grants ST/H008519/1 and ST/K00087X/1, STFC DiRAC Operations grant ST/K003267/1 and Durham University. DiRAC is part of the National E-Infrastructure. This research was supported by the Munich Institute for Astro- and Particle Physics (MIAPP) of the DFG cluster of excellence 'Origin and Structure of the Universe'.

REFERENCES

Ali Z. S. et al., 2015, ApJ, 809, 61
Barkana R., Loeb A., 2001, Phys. Rep., 349, 125
Becker G. D., Bolton J. S., 2013, MNRAS, 436, 1023
Becker G. D., Bolton J. S., Madau P., Pettini M., Ryan-Weber E. V., Venemans B. P., 2015, MNRAS, 447, 3402
Bernardi G. et al., 2009, A&A, 500, 965
Bolton J. S., Puchwein E., Sijacki D., Haehnelt M. G., Kim T.-S., Meiksin A., Regan J. A., Viel M., 2017, MNRAS, 464, 897
Boutsia K. et al., 2011, ApJ, 736, 41
Bowler R. A. A. et al., 2012, MNRAS, 426, 2772
Bowler R. A. A. et al., 2014, MNRAS, 440, 2810
Bowler R. A. A. et al., 2015, MNRAS, 452, 1817
Bowman J. D. et al., 2013, PASA, 30, e031
Bradley L. D. et al., 2014, ApJ, 792, 76
Brook C. B., Stinson G., Gibson B. K., Roškar R., Wadsley J., Quinn T., 2012, MNRAS, 419, 771
Calverley A. P., Becker G. D., Haehnelt M. G., Bolton J. S., 2011, MNRAS, 412, 2543
Chardin J., Haehnelt M. G., Aubert D., Puchwein E., 2015, MNRAS, 453, 2943
Chardin J., Puchwein E., Haehnelt M. G., 2017, MNRAS, 465, 3429
Choudhury T. R., Haehnelt M. G., Regan J., 2009, MNRAS, 394, 960
Choudhury T. R., Puchwein E., Haehnelt M. G., Bolton J. S., 2015, MNRAS, 452, 261
D'Aloisio A., Upton Sanderbeck P. R., McQuinn M., Trac H., Shapiro P. R., 2016, preprint (arXiv:1607.06467v1)
Davies F. B., Furlanetto S. R., 2016, MNRAS, 460, 1328
Dillon J. S. et al., 2014, Phys. Rev. D, 89, 023002
Faucher-Giguère C.-A., Lidz A., Zaldarriaga M., Hernquist L., 2009, ApJ, 703, 1416
Ferrarese L., 2002, ApJ, 578, 90
Finkelstein S. L., 2016, PASA, 33, e037
Finlator K., Oppenheimer B. D., Davé R., Zackrisson E., Thompson R., Huang S., 2016, MNRAS, 459, 2299
Furlanetto S. R., Zaldarriaga M., Hernquist L., 2004, ApJ, 613, 1
Furlanetto S. R., Oh S. P., Briggs F. H., 2006, Phys. Rep., 433, 181
Ghara R., Choudhury T. R., Datta K. K., 2015, MNRAS, 447, 1806
Giallongo E. et al., 2015, A&A, 578, A83
Grazian A. et al., 2016, A&A, 585, A48
Haardt F., Madau P., 2012, ApJ, 746, 125
Haehnelt M. G., Kauffmann G., 2002, MNRAS, 336, L61
Hönig S. F. et al., 2017, MNRAS, 464, 1693
Hopkins P. F., Richards G. T., Hernquist L., 2007, ApJ, 654, 731
Iliev I. T., Mellema G., Shapiro P. R., Pen U.-L., Mao Y., Koda J., Ahn K., 2012, MNRAS, 423, 2222
Japelj J. et al., 2017, MNRAS, 468, 389
Kakiichi K., Graziani L., Ciardi B., Meiksin A., Compostella M., Eide M. B., Zaroubi S., 2016, MNRAS, 468, 3718
Kauffmann G., Haehnelt M., 2000, MNRAS, 311, 576
Kelly B. C., Merloni A., 2012, Adv. Astron., 2012, 970858
Khaire V., Srianand R., Choudhury T. R., Gaikwad P., 2016, MNRAS, 457, 4051
Kuhlen M., Faucher-Giguère C.-A., 2012, MNRAS, 423, 862
Kulkarni G., Loeb A., 2012, MNRAS, 422, 1306
Kulkarni G., Choudhury T. R., Puchwein E., Haehnelt M. G., 2016, MNRAS,
Laureijs R. et al., 2011, preprint (arXiv:1110.3193)
Livermore R. C., Finkelstein S. L., Lotz J. M., 2017, ApJ, 835, 113
Lusso E. et al., 2010, A&A, 512, A34
Lusso E., Worseck G., Hennawi J. F., Prochaska J. X., Vignali C., Stern J., O'Meara J. M., 2015, MNRAS, 449, 4204
Madau P., Haardt F., 2015, ApJ, 813, L8
Majumdar S., Mellema G., Datta K. K., Jensen H., Choudhury T. R., Bharadwaj S., Friedrich M. M., 2014, MNRAS, 443, 2843
Mao J., Kim M., 2016, ApJ, 828, 96
Matsuoka Y. et al., 2016, ApJ, 828, 26
McQuinn M., Furlanetto S. R., Hernquist L., Zahn O., Zaldarriaga M., 2005, ApJ, 630, 643
McQuinn M., Lidz A., Zahn O., Dutta S., Hernquist L., Zaldarriaga M., 2007, MNRAS, 377, 1043
Meiksin A., 2005, MNRAS, 356, 596
Meiksin A., White M., 2004, MNRAS, 350, 1107
Merloni A., Heinz S., 2008, MNRAS, 388, 1011
Mesinger A., Furlanetto S., Cen R., 2011, MNRAS, 411, 955
Micheva G., Iwata I., Inoue A. K., 2017a, MNRAS, 465, 302
Micheva G., Iwata I., Inoue A. K., Matsuda Y., Yamada T., Hayashino T., 2017b, MNRAS, 465, 316
Mitra S., Choudhury T. R., Ferrara A., 2015, MNRAS, 454, L76
Mitra S., Choudhury T. R., Ferrara A., 2016, preprint (arXiv:1606.02719v2)
Mostardi R. E., Shapley A. E., Steidel C. C., Trainor R. F., Reddy N. A., Siana B., 2015, ApJ, 810, 107
Oesch P. A. et al., 2016, ApJ, 819, 129
Parsons A. R. et al., 2014, ApJ, 788, 106
Planck Collaboration XVI, 2014, A&A, 571, A16
Planck Collaboration XLVII, 2016, A&A, 596, A108
Pober J. C. et al., 2013, ApJ, 768, L36
Pober J. C. et al., 2014, ApJ, 782, 66
Pritchard J. R., Loeb A., 2012, Rep. Prog. Phys., 75, 086901
Puchwein E., Bolton J. S., Haehnelt M. G., Madau P., Becker G. D., Haardt F., 2015, MNRAS, 450, 4081
Rahmati A., Pawlik A. H., Raičevič M., Schaye J., 2013, MNRAS, 430, 2427

Ricci F., Marchesi S., Shankar F., La Franca F., Civano F., 2017, MNRAS, 465, 1915
Robertson B. E., Ellis R. S., Furlanetto S. R., Dunlop J. S., 2015, ApJ, 802, L19
Siana B. et al., 2015, ApJ, 804, 17
Spergel D. N. et al., 2003, ApJS, 148, 175
Spergel D. N. et al., 2013, preprint (arXiv:1305.5422)
Springel V., 2005, MNRAS, 364, 1105
Springel V., Yoshida N., White S. D. M., 2001, New A, 6, 79
Srbinovsky J. A., Wyithe J. S. B., 2007, MNRAS, 374, 627
Stark D. P. et al., 2015a, MNRAS, 450, 1846
Stark D. P. et al., 2015b, MNRAS, 454, 1393
Stark D. P. et al., 2017, MNRAS, 464, 469
Telfer R. C., Kriss G. A., Zheng W., Davidsen A. F., Tytler D., 2002, ApJ, 579, 500
Thomas R. M., Zaroubi S., 2008, MNRAS, 384, 1080
Tingay S. J. et al., 2013, PASA, 30, e007
Tremaine S. et al., 2002, ApJ, 574, 740
van Haarlem M. P. et al., 2013, A&A, 556, A2
Vanden Berk D. E. et al., 2001, AJ, 122, 549
Vanzella E. et al., 2010, ApJ, 725, 1011
Wyithe J. S. B., Bolton J. S., 2011, MNRAS, 412, 1926

APPENDIX: AGN-IONIZING EMISSIVITY

In our simulations, AGNs are implemented according to the procedure described in Section 2. In this work, we assume that haloes with mass below a threshold mass $M_{\rm q}$ have $N_\gamma(M) = N_\gamma^{\rm gal}(M) \propto M_{\rm halo}$. Ionizing photons from these low-mass haloes are sourced by star formation. On the other hand, high-mass haloes with mass greater than the threshold $M_{\rm q}$ have $N_\gamma(M) = N_\gamma^{\rm agn}(M) \propto M_{\rm bh}$, where $M_{\rm bh}$ is given by equation (10). These high-mass haloes produce ionizing photons due to AGNs. The ratio r, defined in equation (11), quantifies the relative photon contribution of AGNs and galaxies. Our AGN models are thus described by two parameters r and $M_{\rm q}$. We fix the value of the threshold mass $M_{\rm q}$ to that corresponding to a circular velocity of $v_{\rm c} = 175$ km s^{-1} in our fiducial model, but also consider the effect of varying this threshold to $v_{\rm c} = 150$ km s^{-1} and $v_{\rm c} = 200$ km s^{-1} in Fig. 3. The left-hand panel of Fig. A1 shows the N_γ assignment for AGNs in our fiducial model ($v_{\rm c} = 175$ km s^{-1}) at redshifts $z = 7$, 8 and 10. Below the threshold mass, $N_\gamma \propto M_{\rm halo}$ and above it $N_\gamma \propto M_{\rm bh} \propto M_{\rm halo}^{1.6}$, following equation (10). The middle panel of Fig. A1 shows N_γ as a function of the halo circular velocity. We see that N_γ sharply increases at $v_{\rm c} = 175$ km s^{-1}. This velocity corresponds to a different halo mass at each of the three redshifts considered here, as seen in the right-hand panel of Fig. A1. The magnitude of N_γ increases with redshift to compensate for the decreasing number density of haloes above the velocity threshold. As described in Section 2, where we discuss our calibration procedure, the required total ionizing emissivity is dictated by our chosen reionization model.

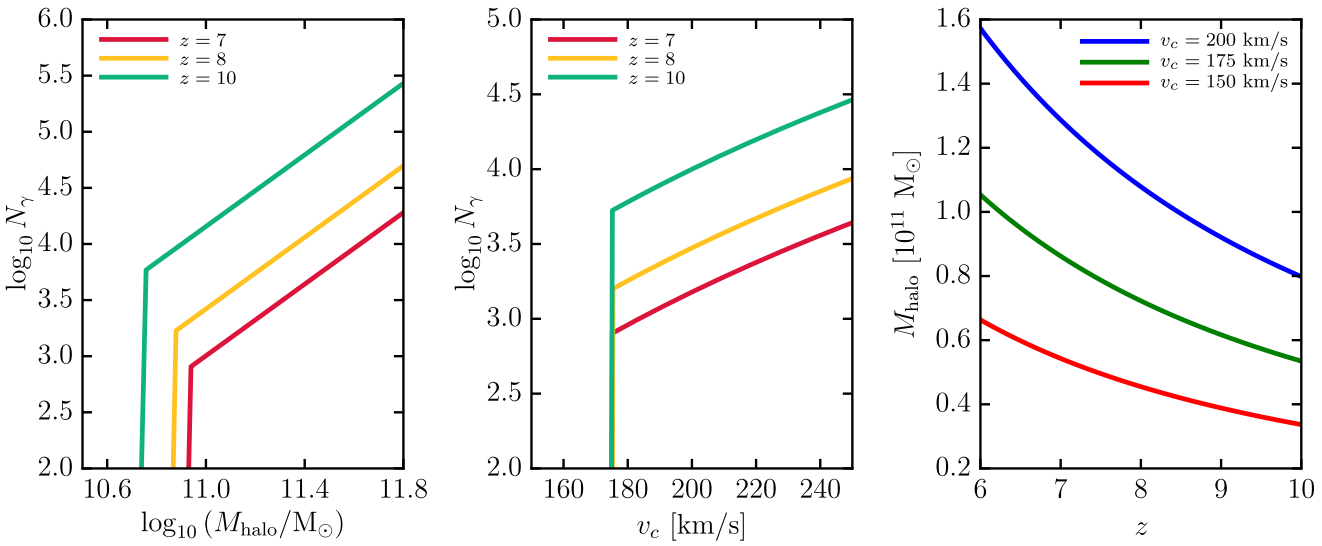

Figure A1. Our model for the photon contribution N_γ for AGNs at various redshifts as a function of halo mass (left-hand panel) and circular velocity (middle panel). The right-hand panel shows the evolution of halo mass corresponding to the three circular velocity thresholds considered in this paper. Our chosen reionization model dictates the amplitude of the N_γ–$M_{\rm halo}$ relation, while its slope is governed by the black hole mass model of equation (10).

This paper has been typeset from a TEX/LATEX file prepared by the author.